Assessment of Pioneer Venus Entry Heating with Coupled Radiation and Ablation

Jannuel V. V. Cabrera* and Thomas K. West IV†
NASA Langley Research Center, Hampton, VA, 23681

The objective of this work is to reconstruct thermocouple temperature measurements taken at the stagnation point of the Pioneer Venus large probe using uncoupled and coupled ablation calculations. The time history of the large probe forebody entry heating was obtained from a trajectory-based analysis that employed a material response solver to model equilibrium and nonequilibrium ablation chemistry at the surface. In the uncoupled approach, equilibrium ablation chemistry was assumed in the material response calculations, but the material response outputs were not returned to the flowfield solver. Therefore, the effects of char and pyrolysis gas injection into the boundary layer due to ablation (e.g., convective blockage and radiative energy absorption) did not influence the flowfield solutions. In the coupled approach, nonequilibrium ablation chemistry was performed and the material response outputs were returned to the flowfield solver. Therefore, the effects of char and pyrolysis gas injection into the boundary layer were accounted for in the flowfield solutions. Both uncoupled and coupled approaches produced reconstructed temperatures that were within 10% of the flight measurements through the entry heat pulse, with the coupled results comparing more favorably with the measurements. Overall, the reconstructed thermocouple temperatures in this work significantly improved on the results of previous reconstructions for the large probe.

I. Introduction

On December 9, 1978, the four Pioneer Venus probes designated as day, large, night, and north, entered the atmosphere of Venus to take measurements for the construction of an improved atmospheric model [1]. The probes entered the Venusian atmosphere at 11.54 km/s and at entry angles between -25 deg and -69 deg. During the high-velocity entries into the dense atmosphere, the severe aerodynamic heating produced shock layer temperatures exceeding 10,000 K. The response of the carbon phenolic thermal protection system (TPS) to the extreme entry environments of the probes was measured via two thermocouples embedded in each probe: one in the stagnation region at a depth of 0.41 cm from the heated surface and one on the conical flank at a depth of 0.30 cm. The experiment was intended to aid heat shield design efforts for the Galileo probe, which also used a carbon phenolic heat shield.

Studies were performed ahead of the Pioneer Venus mission to characterize the entry heating environment expected for the probes. In 1972, Page and Woodward estimated the convective and radiative heat fluxes at the stagnation point of a Venus probe as a function of flight velocity, shock standoff distance, and shock layer pressures [2]. In their analysis, heat shield ablation was ignored, thereby neglecting convective and radiative blockage. Later in 1974, Sutton generated solutions that modeled coupled radiation and ablation at the peak radiative heating points during a sample entry trajectory into the Venusian atmosphere [3]. In that work, Sutton assumed that the virgin and charred carbon phenolic receded at the same linear rate (steady-state ablation) and found that the radiative heat flux at the surface was reduced by 10% to 20% due to self-absorption of the carbon monoxide fourth positive band system (CO 4^{th} Positive). A comprehensive trajectory-based analysis of the entry heating was published by Moss et al. in 1977 [4]. Their analysis modeled a viscous shock layer with equilibrium surface chemistry and ablation species injection at specified rates. Radiative heating at the wall was reduced through absorption, mainly by CO, as previously observed by Sutton. Additionally, Moss et al. found that convective blockage was significant due to carbon phenolic injection. The convective blockage reduced the convective heat flux at the stagnation point and conical flank by 88% and 58%, respectively, relative to non-ablating calculations. Both Refs. [3] and [4] demonstrated that modeling ablation in the flowfield solution is necessary to avoid overpredicting the heating environment.

In 1980, Wakefield and Pitts published the first post-flight reconstruction of the thermocouple measurements [5]. Because trajectory data was not yet available for the large and night probes, their reconstruction effort focused on the

*Aerospace Engineer, Vehicle Analysis Branch, Systems Analysis and Concepts Directorate.
†Aerospace Engineer, Vehicle Analysis Branch, Systems Analysis and Concepts Directorate, Member AIAA.

north and day probes. The Charring Material Ablation (CMA) computer program was used to calculate the in-depth temperature distribution within the carbon phenolic heat shields, assuming that the pyrolysis and boundary layer gases were in chemical equilibrium. They used the approximate methods of Zoby et al. [6] and Falanga et al. [7] to compute time histories for the convective and radiative heat fluxes, respectively. Note that the material response and surface heat flux calculations were uncoupled. For the day probe, Wakefield and Pitts' calculated thermocouple temperature rise slope compared well with the flight measurements, but a 2-3 s offset in the temperature rise time was observed. They cited uncertainty in the entry times of the probes as the potential cause of the timing discrepancy. For the north probe, their calculated temperature rise slope did not match that of the data and they calculated temperatures that significantly overpredicted the measured data at the stagnation region. Wakefield and Pitts suggested that the north probe heating rates provided to the CMA code may have been larger than those experienced during flight. They suggested that incorporating ablation effects, like radiative blockage, in further analysis could resolve the discrepancy.

Almost two decades later, Ahn et al. performed a reconstruction of the flight measurements at the stagnation region of all four probes using the Super Charring Materials Ablation (SCMA) material response code [8]. They used the method described by Park and Ahn to compute the convective and radiative heat rates [9]. Radiation transport was modeled using a line-by-line technique and the tangent slab approximation. Nonequilibrium (finite-rate) ablation chemistry was also modeled for gas-gas and gas-surface interactions. Instead of assuming steady-state ablation, where the ratio of carbon char vaporization rate to pyrolysis gas injection rate is fixed, time-dependent pyrolysis gas injection rates were calculated and returned to the flowfield calculations in a coupled manner. Coupling enabled convective and radiative blockage by ablation species to be incorporated into the flowfield analysis. Compared to the earlier results of Wakefield and Pitts, Ahn et al. showed improved agreement between flight data and computations for the day and north probes. They noted that the similarity in the slopes of the measured and calculated temperature rise implied that the rate of energy transfer was being modeled correctly. The same 2-3 s offset in the temperature rise observed by Wakefield and Pitts persisted, and Ahn et al. also attributed this to potential inaccuracy in the entry times initially reported for the probes. The calculated thermocouple temperatures for the large and night probes appeared to exceed the measurements by as much as 250 K and the temperature rise slopes did not compare well with the flight data. Ahn et al. attributed the error to the lack of a confirmed entry trajectory for either probe due to missing accelerometer data.

Soon after the work of Ahn et al., Takahashi and Sawada performed a reconstruction in which they calculated temperatures at both the stagnation point and the flank thermocouple locations [10]. They used the CMA material response code and performed coupled ablation calculations that assumed nonequilibrium ablation chemistry. They also employed an injection-induced turbulence model to simulate a fully turbulent boundary layer over the entire surface of each probe. Fair comparisons to the flight data were drawn for the north and day probes, but poorer comparisons were observed for the large and night probes. The rise time offsets observed by Ahn et al. recurred in Takahashi and Sawada's investigation.

The objective of this work is to reconstruct thermocouple temperature measurements taken at the stagnation point of the Pioneer Venus large probe using uncoupled and coupled ablation calculations. The entry heating environment was determined from a trajectory-based analysis. For the uncoupled ablation approach, equilibrium ablation chemistry was assumed and the flowfield was solved separately from the material response calculations. In the coupled approach, nonequilibrium, finite-rate ablation chemistry was modeled and the flowfield calculations were coupled to the material response calculations. The large probe was chosen for this analysis because its dimensions are comparable to those of the probe scheduled to fly on NASA's upcoming Deep Atmosphere Venus Investigation of Noble gases, Chemistry, and Imaging (DAVINCI) mission [11].

The organization of this paper is as follows. Section II describes the modeling approach to perform uncoupled and coupled flowfield-material response calculations. Section III presents the calculated entry heating environment of the large probe and also compares the reconstructed stagnation point thermocouple temperatures with flight measurements. Lastly, concluding remarks are given in Sec. IV.

II. Simulation Approach

This section describes the geometry and trajectory of the large probe as well as the flowfield and material response modeling approaches.

A. Probe Geometry and Trajectory

The probes were spherically blunted cones with a 45 deg half-angle, as sketched in Fig. 1. The large probe had a base radius (R_b) of 0.71 m and a nose radius (R_n) of 0.355 m. Two thermocouples were installed in the following

locations on the probe: 0.41 cm below the heated surface at the stagnation point (Z of 0 m and S/R_n of 0 in Fig. 1) and 0.30 cm below the heated surface at the conical flank (Z of 0.614 m and S/R_n of 2.2 in Fig. 1). The nominal thicknesses of the heat shield at the stagnation and flank regions were 1.0 cm and 0.70 cm, respectively.

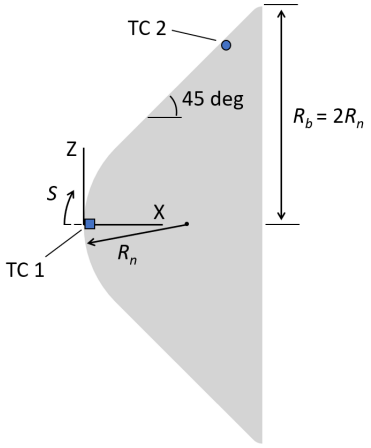

Fig. 1 Pioneer Venus forebody sketch with large probe thermocouple locations.

The entry heating history required by the material response solver was obtained by calculating the forebody flowfield corresponding with the reconstructed trajectory points summarized in Table 1. The flight times listed are referenced to the probe's passing of the reference altitude, which is defined as 200 km relative to the large probe's landing site [1]. Flight conditions between 18.0 s and 20.4 s were directly adopted from the work of Tauber et al. [12]. The trajectory points from 21.5 s to 24.5 s were obtained by reconstructing a ballistic trajectory (zero angle of attack) via numerical integration of the three degree-of-freedom equations of motion for planar entry flight. The initial conditions for entry altitude, velocity, and flight path angle used in the reconstruction were 137.78 km, 11.584 km/s, and -31.829 deg, respectively; note that these were the same initial conditions used by Tauber et al. to calculate the trajectory points between 18.0 s and 20.4 s. The corresponding atmospheric density and temperature profiles were based on the flight measurements reported by Seiff et al. [1]. Lastly, a ballistic coefficient of 190 kg/m^2 was assumed in the trajectory reconstruction [12].

Table 1 Reconstructed large probe trajectory

Time, s	Altitude, km	Velocity, m/s	Density, kg/m^3	Temperature, K
18.0	89.24	11310	1.39×10^{-3}	165.3
18.6	85.77	10880	3.26×10^{-3}	163.9
18.8	84.65	10651	4.24×10^{-3}	164.4
19.2	82.49	10028	6.92×10^{-3}	177.5
19.5	80.98	9408	9.64×10^{-3}	188.6
19.7	80.02	8927	1.18×10^{-2}	195.7
20.0	78.69	8134	1.55×10^{-2}	210.5
20.4	77.12	7015	2.13×10^{-2}	214.9
21.5	73.84	4435	3.78×10^{-2}	227.4
22.5	71.96	2895	5.30×10^{-2}	233.6
23.5	70.71	1988	6.64×10^{-2}	237.4
24.5	69.82	1450	7.75×10^{-2}	241.2

B. Flowfield Model

The Langley Aerothermodynamic Upwind Relaxation Algorithm (LAURA) Navier-Stokes flow solver [13] was used to perform axisymmetric forebody flowfield calculations. The finite-volume solver employs a second-order upwind discretization scheme with Roe's flux-difference splitting scheme as well as Yee's symmetric total variation diminishing (STVD) formulation of the inviscid flux [14]. The flowfield was modeled with a two-temperature thermochemical nonequilibrium assumption. The freestream gas composition was modeled as 97.4% CO_2 and 2.6% N_2 by mass. The Cebeci-Smith algebraic turbulence model was employed to simulate a fully turbulent boundary layer [15]. Twenty-nine chemical species were included in the flowfield calculations: C, C_2, C_3, C_4, C_5, CN, CO, CO_2, C^+, CO^+, N, N_2, NO, N^+, NO^+, O, O_2, O^+, CH, C_2H, CH_2, CH_3, CH_4, C_2H_2, H, H_2, HCN, H^+, and e^-. The chemical kinetic rate model of Johnston and Brandis was employed in this work [16]. Axisymmetric computational grids with 40 cells along the surface and 80 cells normal to the wall were used. A brief sensitivity study revealed that doubling these grid dimensions changed the stagnation point convective and radiative heat fluxes by only 0.09% and 0.05%, respectively. This insignificant change in heating was deemed not worth the increase in computational burden and thus the 40×80 grid was utilized. Shock alignment was performed via grid adaptions that targeted a cell Reynolds number of 1.0. Note that ablation-induced wall recession can change the forebody shape, and thus its heating, as shown for the Galileo probe by Erb et al. [17]. However, preliminary calculations performed in this work showed that the recession at the stagnation point was only 20% of the Galileo result. This smaller recession was deemed to have a small impact on the forebody heating. Therefore, deformation of the computational grid due to recession was not modeled in this work.

Shock layer radiation was calculated using the High-Temperature Aerothermodynamic Radiation (HARA) code [18]. The coupling of the radiative energy transport to the flowfield calculations was achieved by using the tangent slab approximation to compute the divergence of the radiative flux (∇q_r). A ray tracing approach [19] was utilized to compute the surface radiative heat fluxes instead of the tangent slab approach. Lastly, the radiation mechanisms of C, C_2, C_3, C_2H, CN, CO, N, N_2, and O were modeled [16, 20].

C. Material Response Model

Uncoupled and coupled material response calculations were carried out using a one-dimensional material response solver based on the formulation of Amar [21] built into LAURA. The solver computes the pyrolysis gas mass flux injected into the flowfield, the heat conducted into the material, and the gas composition using time histories of the wall temperature and heat fluxes from the flowfield calculations. The coupling between the ablating surface and the flowfield is treated by solving the surface energy balance and species mass balance equations. The surface energy balance equation is written as follows:

$$q_c + \alpha q_{\text{rad}} - \epsilon\sigma T_w^4 - \dot{m}_c(h_w - h_c) - \dot{m}_g(h_w - h_g) - q_{\text{cond}} = 0 \tag{1}$$

where q_c is the convective heat flux, α is the absorptivity of the surface (assumed to be 0.7 [5]), q_{rad} is the radiative heat flux, ϵ is the emissivity of the surface (assumed to be 0.7 [5]), σ is the Stefan-Boltzmann constant*, T_w is the wall temperature, $\dot{m}_c$ is the char mass flux, $\dot{m}_g$ is the pyrolysis gas mass flux, h_w is the specific enthalpy of the gas at the wall, h_c is the solid char specific enthalpy, h_g is the pyrolysis gas specific enthalpy, and q_{cond} is the heat rate conducted into the heat shield. The species mass balance equation for the species k at the ablating surface is written as follows:

$$J_k + \left(\sum_j \dot{m}_{c,j} + \dot{m}_g\right) c_{w,k} - \dot{m}_{c,k} - \dot{m}_g c_{g,k} = 0 \tag{2}$$

where $c_{g,k}$ and $c_{w,k}$ are the species compositions of the pyrolysis and wall gases, respectively. The $c_{g,k}$ values are computed by assuming that the pyrolysis gases are in chemical equilibrium at the surface temperature before reaching the boundary layer. J_k is the diffusive flux of species k. The $\dot{m}_{c,k}$ values are the individual species mass fluxes due to finite rate surface reactions. The finite rate surface reactions modeled in this work are described later in Sec. II.D. Note that in the case of coupled equilibrium ablation, the solution of the species mass balance reduces to solving the elemental mass balance at the wall. The procedures employed to solve Eqs. (1)-(2) are described in more detail in Refs. [18, 21, 22].

In the uncoupled approach, the ablating surface and the boundary layer gases are assumed to be in chemical equilibrium. Therefore, an equilibrium ablation model was utilized. For the uncoupled ablation calculations, radiating but non-ablating flowfield solutions with fully catalytic walls in radiative equilibrium were computed. These non-ablating solutions provided the heat transfer coefficient, wall enthalpy and pressure, and radiative heating needed by an equilibrium

*The value of σ is 5.67037×10^{-8} W/(m^{2}K^4)

ablation model, which then computed $\dot{m}_c$, $\dot{m}_g$, and T_w. The equilibrium ablation model employed the following heat transfer coefficient correction to account for the effect of char blowing on the convective heating:

$$C_H = C_{H,0}\frac{2\lambda B_0}{\exp(2\lambda B_0) - 1} \tag{3}$$

where C_H is the corrected heat transfer coefficient, $C_{H,0}$ is the heat transfer coefficient returned by the non-ablating flowfield solution, λ is a correction factor used to model laminar or turbulent flows, and B_0 is the blowing parameter, which is a function of the densities and velocities at the wall and boundary layer edge. In this work, λ was set equal to 0.4 because the boundary layer was assumed to be fully turbulent. B_0 was determined from pre-computed tables (also known as B-prime tables). C_H was then used to compute a corrected convective heat flux through the equation:

$$q_c = C_H(H_T - h_w) \tag{4}$$

where H_T is the total enthalpy. The mass transfer coefficient is assumed to equal C_H in an uncoupled approach, thereby enabling the elemental mass balance at the wall to be solved algebraically. Additionally, the outputs returned by the material response solver were not used to update the flowfield. The uncoupled ablation approach is often referred to as the B-prime approach.

For coupled flowfield-material response calculations, the $\dot{m}_g$ and gas composition returned by the material response solver were used to update the wall boundary conditions of the flowfield solutions. Additionally, the boundary layer gas and ablating surface were no longer assumed to be in chemical equilibrium as finite rate (nonequilibrium) chemistry was imposed at the wall. With each update from the material response solver, the wall temperature was iteratively updated via a solution of the surface energy balance during the flowfield calculations for each trajectory point. Note that the surface char rate was determined by the flow solver. After T_w stopped changing during the flowfield solution, the material response solver was called again to update the pyrolysis gas blowing rate and the heat conduction through the material. This iterative procedure was repeated until T_w and the blowing rates converged. The thermocouple temperature history was also monitored between material response updates and when the thermocouple temperatures no longer changed, the calculation was considered finished.

D. Surface Chemistry Models

The coupled flowfield-material response calculations assumed finite rate (nonequilibrium) surface chemistry. The finite rate chemical reactions induced by the ablating surface were the oxidation, sublimation, and nitridation of solid carbon. The two oxidation reactions considered in this work were O + C(s) $\rightarrow$ CO and O_2 + 2C(s) $\rightarrow$ 2CO and the corresponding forward rates are written as follows:

$$k_{f,\mathrm{O}} = \gamma_{\mathrm{O}}\sqrt{\frac{RT}{2\pi M_{\mathrm{O}}}} \tag{5}$$

$$k_{f,\mathrm{O2}} = \gamma_{\mathrm{O2}}\sqrt{\frac{RT}{2\pi M_{\mathrm{O2}}}} \tag{6}$$

where $\gamma_{\mathrm{O}} = 0.63\exp(-1160/T)$ and $\gamma_{\mathrm{O2}} = (0.00143 + 0.01\exp(-1450/T))/(1 + 0.0002\exp(13000/T))$, as suggested by Park [23]. The species mass fluxes resulting from these processes are:

$$\dot{m}_{\mathrm{CO}} = \frac{M_{\mathrm{CO}}}{M_{\mathrm{O}}}k_{f,\mathrm{O}}\,\rho_{\mathrm{O}} + 2\frac{M_{\mathrm{CO}}}{M_{\mathrm{O_2}}}k_{f,\mathrm{O_2}}\,\rho_{\mathrm{O_2}} \tag{7}$$

$$\dot{m}_{\mathrm{O}} = -k_{f,\mathrm{O}}\,\rho_{\mathrm{O}} \tag{8}$$

$$\dot{m}_{\mathrm{O_2}} = -k_{f,\mathrm{O_2}}\,\rho_{\mathrm{O_2}} \tag{9}$$

where ρ_i and M_i are the densities[†] and molecular weights[‡], respectively, of the species in the corresponding subscripts in Eqs. (7)-(9).

[†]Units of kg/m^3

[‡]Units of kg/mol

Four sublimation reactions were also considered:

$$\mathrm{C(s)} \rightarrow \mathrm{C} \tag{10}$$

$$2\mathrm{C(s)} \rightarrow \mathrm{C_2} \tag{11}$$

$$3\mathrm{C(s)} \rightarrow \mathrm{C_3} \tag{12}$$

$$5\mathrm{C(s)} \rightarrow \mathrm{C_5} \tag{13}$$

The sublimation rates are written as:

$$\dot{m}_{\mathrm{C}_i} = \alpha_{\mathrm{C}_i} \left(p_{E,\mathrm{C}_i} - p_{\mathrm{C}_i} \right) \sqrt{\frac{RT}{2\pi M_{\mathrm{C}_i}}} \tag{14}$$

where the subscript i indicates the corresponding reaction in Eqs. (10)-(13) and $p_{E,\mathrm{C}_i} = A_i T^{N_i} \exp(-E_i/T)$ is the equilibrium vapor pressure in N/m^2. The coefficients for p_{E,C_i} [24] and the values of α_{C_i} [25] are listed in Table 2.

Table 2 Sublimation rate coefficients

C_i	α_i	A_i	N_i	E_i
C	0.140	1.029×10^{15}	-0.487	-8.711×10^{4}
$\mathrm{C_2}$	0.260	6.388×10^{19}	-1.318	-1.017×10^{5}
$\mathrm{C_3}$	0.030	9.976×10^{24}	-2.459	-1.033×10^{5}
$\mathrm{C_5}$	0.015	4.600×10^{17}	-0.266	-1.170×10^{5}

The nitridation reaction considered was N + C(s) $\rightarrow$ CN, for which the forward rate is written as:

$$k_{f,\mathrm{N}} = \gamma_{\mathrm{N}} \sqrt{\frac{RT}{2\pi M_{\mathrm{N}}}} \tag{15}$$

where γ_{N} was set to 0.001 as suggested by Driver and MacLean [26]. The corresponding mass flux equations are:

$$\dot{m}_{\mathrm{CN}} = \frac{M_{\mathrm{CN}}}{M_{\mathrm{N}}} k_{f,\mathrm{N}} \, \rho_{\mathrm{N}} \tag{16}$$

$$\dot{m}_{\mathrm{N}} = -\left(k_{f,\mathrm{N}} + \gamma_{\mathrm{Nr}} \sqrt{\frac{RT}{2\pi M_{\mathrm{N}}}} \right) \rho_{\mathrm{N}} \tag{17}$$

Note that in Eq. (17), γ_{Nr} is 0.05 according to Driver and MacLean [26].

E. Material Properties Investigation

In the literature, there is a lack of consensus on the exact thermal properties corresponding with the carbon phenolic used on the probes (see for example, Refs. [5, 27]). In their reconstruction of the large probe stagnation point thermocouple temperatures, Ahn et al. [8] adopted the thermal conductivity values proposed by Wakefield and Pitts [5]. However, Ahn et al.'s calculated temperature rise for the large probe does not compare well with the flight data. Because the material properties used in Ref. [8] did not yield favorable comparisons with the flight measurements, preliminary uncoupled material response calculations were performed to identify the material property model that could qualitatively reproduce the temperature rise slope measured by the large probe's stagnation point thermocouple. For this preliminary investigation, the carbon phenolic thermal conductivity values reported by Wakefield and Pitts [5], Peterson and Nicolet [27], Brewer [28], and Sutton [29] were used. The thermal conductivity values for the carbon phenolic char material from these reports are compared in Fig. 2(a). The enthalpies of the virgin plastic, char material, and pyrolysis gas reported by Peterson and Nicolet, and the carbon phenolic decomposition kinetic rates reported by Rindal et al. [30] were temporarily adopted to complete the material model used in the preliminary investigation of the temperature rise slope.

The thermocouple temperatures obtained from the preliminary investigation are shown in Fig. 2(b), where the four curves correspond to the four sources of thermal conductivity values mentioned previously. Peterson and Nicolet's

[27] and Wakefield and Pitts' [5] thermal conductivity values produced sharper increases in the temperature. Although Brewer's [28] data yielded milder discrepancies with the flight data, temperature differences over 200 K can still be observed. Figure 2(b) shows that using the thermal conductivity data from Sutton [29] yielded the temperature rise slope that compared most favorably with the flight measurements. Therefore, Sutton's thermal conductivity values for both the virgin plastic and char material were employed in the final material model used in all calculations performed after this preliminary investigation. Note that previous reconstruction efforts for the large probe noticed that the computed temperature rise occurred 2-3 s ahead of the measurements [8, 10]. Using Sutton's data revealed no such discrepancy in Fig. 2(b), which added confidence to the adoption of his thermal conductivity data for all subsequent calculations. Additionally, the enthalpies of the virgin plastic, char material, and pyrolysis gas provided by Sutton were also used in the final material model for consistency. The decomposition kinetic rates provided by Rindal et al. [30] were again used in the final material model. The char composition (100% C by mass) and pyrolysis gas composition (38.8% C, 17.8% H, and 43.4% O by mass) were adopted from Wakefield and Pitts because these values were unavailable from Sutton's report. The final material model is presented in the appendix.

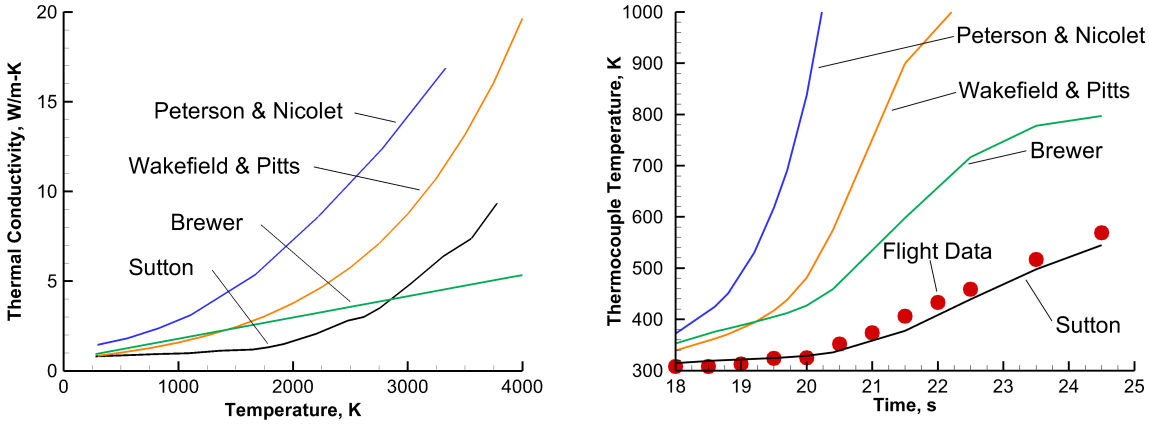

(a) Char thermal conductivity

(b) Thermocouple temperature

Fig. 2 Investigation of different carbon phenolic thermal conductivity values.

III. Results and Discussion

In this section, the impact of coupling the flowfield and material response calculations on the entry heating environment is described. In the following discussion, references to coupled ablation imply the use of finite rate (nonequilibrium) ablation calculations, whereas uncoupled ablation refers to equilibrium ablation. Later in the section, the reconstructed thermocouple temperatures at the stagnation point of the large probe are compared with the flight measurements.

A. Impact of Coupled Ablation

Performing finite rate (nonequilibrium) ablation chemistry instead of equilibrium ablation enabled the modeling of oxidation, sublimation, and nitridation processes near the wall. Known radiative energy contributors (C_2, C_3, C_2H, and CN) were formed due to these reactions in the boundary layer. The number densities of these species near the wall along the stagnation streamline are presented in Fig. 3(a) for the peak radiative heating trajectory point (18.6 s). There is an orders-of-magnitude increase associated with C_2, C_3, C_2H, and CN near the wall due to ablation, but less than an order of magnitude decrease in CO due to ablation (note that C_2H is not formed in the non-ablating solution).

The absorption of radiation near the wall can be inferred from Fig. 3(b), which plots the radiative flux along the stagnation streamline for the 18.6 s case. Note that surface blowing due to ablation increases the shock standoff distance, which explains why the dashed curve appears shifted to the right compared to the solid curve. As expected, the radiation reaching the wall is lowered for the nonequilibrium ablation case. To identify the radiation mechanisms contributing to

the absorption of radiative energy near the wall, the spectral range at the stagnation point was compared between the non-ablating and ablating solutions. As shown in Fig. 3(c), there is a sizable attenuation of the monochromatic heat flux occurring in the 6 eV to 9 eV range due to ablation (red solid line below the black solid line in this range). This eV range corresponds with the C_3 [18] and CO 4th Positive [3] band systems, which were found to account for nearly all absorption at the 18.6 s case. The absorption decreases the cumulative radiative heat flux reaching the wall (red dashed line below the black dashed line). The cumulative impact of these two absorbing species was to reduce the stagnation point radiative heat rate from 2275 W/cm^2 (non-ablating value) to 2027 W/cm^2 (nonequilibrium ablation value), which is an 11% decrease. Regarding Fig. 3, the radiative heating environment shown only applies to the 18.6 s case because the radiation mechanisms impacting the wall-directed radiative flux change with the flow conditions, as demonstrated by West and Brandis [31].

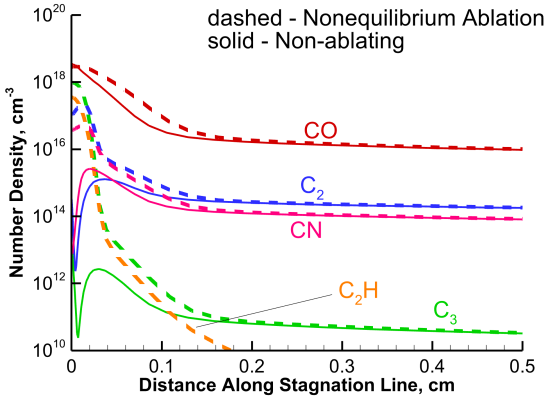

(a) Stagnation line number density

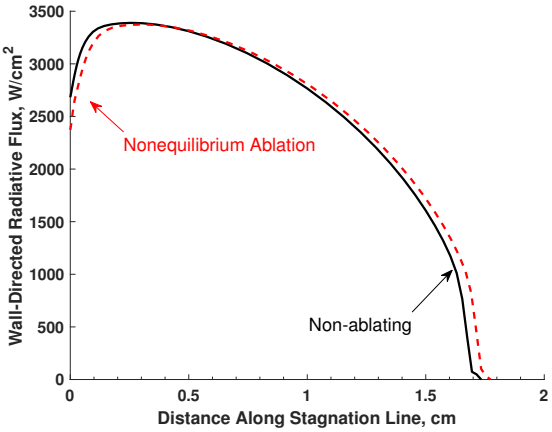

(b) Stagnation line wall-directed flux

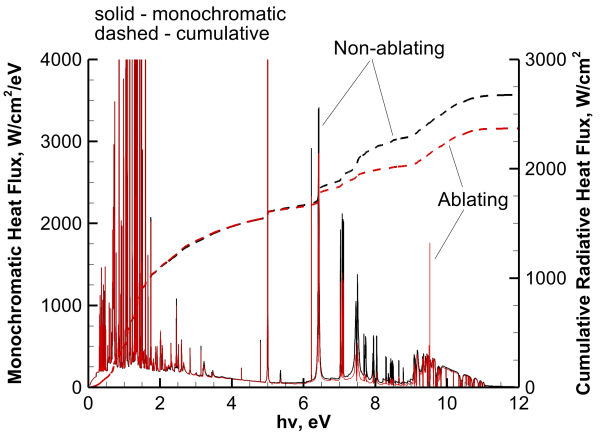

(c) Stagnation line spectral range

Fig. 3 Impact of coupled ablation on stagnation line radiation (18.6 s trajectory point).

The impact of uncoupled and coupled ablation modeling on the surface heating environment is presented in Fig. 4. In Fig. 4(a), the convective and radiative heat flux at the stagnation point through the entry heat pulse are shown. During the earlier portion of the heat pulse when radiation is most significant, the stagnation point radiative heating returned by the uncoupled analysis is greater than the coupled values. At the peak radiative heating trajectory point (18.6 s), the stagnation point radiative heat flux values that resulted from the uncoupled and coupled analyses are 2275 W/cm^2 and 2027 W/cm^2, respectively. As previously discussed, the reduction in the radiative heat flux seen for the coupled results is due to the radiative energy absorption that is being modeled in the coupled calculations.

As for the stagnation point convective heat flux, Fig. 4(a) shows that the uncoupled, blowing-corrected value (recall

Eq. (4)) is lower than the coupled result. At the peak convective heating conditions (19.2 s), the uncoupled and coupled stagnation point convective heat fluxes are 968 W/cm^2 and 1382 W/cm^2, respectively. This reduction in convective heating due to the blowing correction is related to the massive charring predicted by the equilibrium ablation model. As shown in Fig. 4(b), the uncoupled char mass fluxes are greater than the coupled values throughout the entry heat pulse. At 19.2 s, the uncoupled and coupled char rates are 0.97 kg/(m^2-s) and 0.34 kg/(m^2-s), respectively. The greater charring predicted by the equilibrium ablation model translates to more mass being ejected from the ablating surface and into the boundary layer, which significantly reduced the convective heat flux at the stagnation point. The pyrolysis rates are also presented in Fig. 4(b). In general, the pyrolysis rates are smaller than the char rates in both the uncoupled and coupled cases. Note that the pyrolysis gases injected into the boundary layer also contribute to the convective and radiative blockage.

The differences in blowing yields reduced wall temperatures for the uncoupled cases as shown in Fig. 4(c). The peak stagnation point wall temperature in the uncoupled case is 3930 K and occurs at around 20 s. In the case of coupled ablation, the peak wall temperature is 4032 K, which occurs at around 19.5 s. At such temperatures, the sublimation of carbon becomes significant in the case of nonequilibrium ablation, thereby increasing C_3 in the boundary layer. As described earlier, the presence of C_3 in the boundary layer contributes radiative energy absorption.

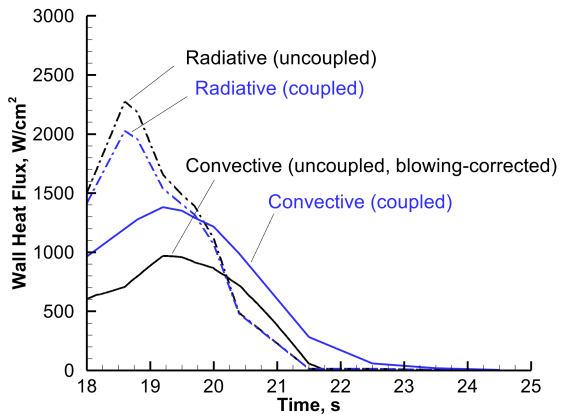

(a) Wall heat flux

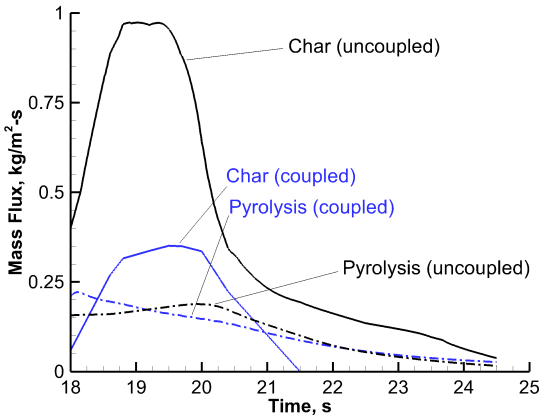

(b) Mass flux

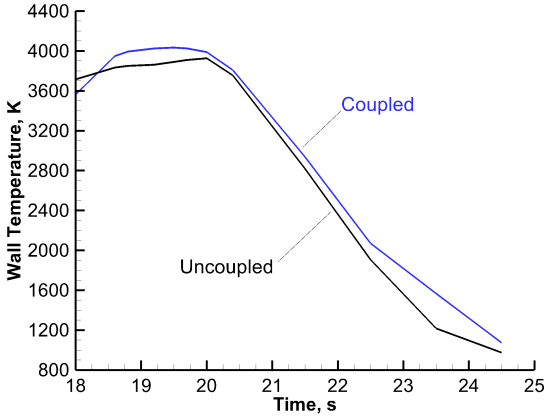

(c) Wall temperature

Fig. 4 Impact of uncoupled and coupled ablation on the stagnation point heating environment.

B. Thermocouple Temperature Reconstruction

After the convergence of the non-ablating flowfield solutions and the coupled ablation calculations, the material response solver was employed one final time to obtain the temperature distribution within the carbon phenolic material. The temperature at a depth of 0.41 cm from the outer heated surface was extracted for comparison with the flight measurements. These reconstructed temperatures from the uncoupled and coupled calculations are shown in Fig. 5.[§] Throughout the heat pulse, the maximum discrepancy between the uncoupled results and measurements is 42 K (10% underprediction), which occurs at the 21.5 s trajectory point. The higher char rates predicted by the uncoupled ablation calculations meant that there was lower incident heating at the wall, previously noted in Fig. 4. In turn, there was less energy being conducted into the surface, which led to the uncoupled calculation underpredicting the flight data. As for the coupled ablation results, there was a maximum discrepancy of 24 K (6% underprediction) that also occurs at the 21.5 s trajectory point. Over the entire heat pulse, Fig. 5 shows that the coupled calculations yield the best comparison with flight data. Here, the excellent agreement is viewed as the result of modeling the finite rate ablation chemistry, which yielded a more accurate heating environment, and using a material model that was deemed most representative of the heat shield material used on the probes.

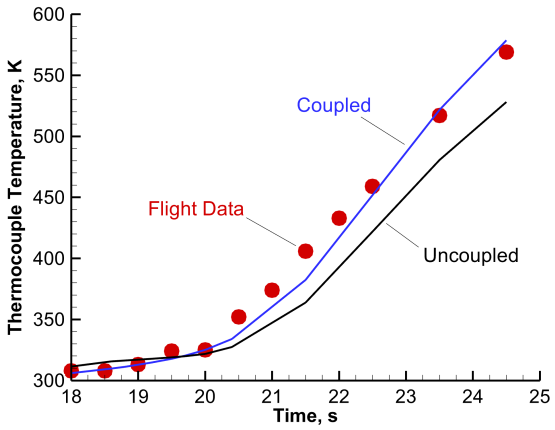

Fig. 5 Reconstructed stagnation point thermocouple temperatures compared with flight data.

IV. Conclusions

This work reconstructed the stagnation point thermocouple temperatures for the Pioneer Venus large probe using uncoupled and coupled ablation calculations. The probe's entry heating environment was calculated with a trajectory-based analysis using a material response solver that modeled equilibrium and nonequilibrium ablation. In the uncoupled approach, equilibrium ablation chemistry was performed and the material response was calculated in a single post-processing step after obtaining converged non-ablating flowfield solutions throughout the trajectory. In the coupled approach, nonequilibrium, finite rate ablation chemistry was performed and the coupling of the flowfield and material response calculations was performed as follows. The flowfield at each trajectory point was used by the material response solver to compute the ablation of the material. Then, the material response results were used to update the flowfield wall boundary conditions. Afterwards, the flowfield solutions were re-converged for the entire trajectory and the updated flowfields were again returned to the material response solver to obtain updated wall boundary conditions. This iterative procedure was repeated until the blowing rates, wall temperature, and heat fluxes converged for each trajectory point.

Given the age of the mission, there is an uncertainty in the actual material properties that is exacerbated by inconsistent and limited information in the literature regarding the carbon phenolic material used on the large probe. The current study utilized an assembly of the best estimate of properties that enabled the replication of the measured stagnation point thermocouple temperature rise for the large probe. Using Sutton's thermal conductivity values was found to be a key factor in replicating the measured temperature rise slope. Employing the updated material properties to calculate thermocouple temperatures for the other probes is the subject of ongoing work.

[§]The corresponding raw values are also tabulated in Tables A1 and A2.

The stagnation point thermocouple temperatures calculated for the large probe were in excellent agreement with the flight data and an improvement over previous reconstruction efforts [5, 8, 10]. In this work, the coupled ablation calculations produced the best comparison with flight measurements. The uncoupled ablation calculations underpredicted the measured data by up to 10% through the heat pulse. This underprediction was suspected to be the result of lowered incident wall heating due to the larger char rates predicted by the equilibrium ablation model used by the uncoupled approach. Modeling nonequilibrium ablation in the coupled calculations led to lower mass flux values that appeared to be more representative of the heating environment experienced by the large probe. As a result, the thermocouple temperatures predicted by the coupled calculations compared better with the flight measurements, with 6% maximum error being observed. The improvement in modeling fidelity appears to have resolved the timing error identified in earlier reconstruction efforts [5, 8, 10]. As demonstrated in this work, the higher-fidelity coupled flowfield-material response approach can improve predictive accuracy. Furthermore, the high-fidelity approach described here can be applied in heat shield sizing efforts on future planetary entry missions, provided that the material properties can be determined.

Appendix

A. Thermocouple Temperatures

Below are the measured and predicted thermocouple temperatures for the Pioneer Venus large probe.

Table A1 Measured stagnation point thermocouple temperatures for the large probe [5]

Time, s	Temperature, K
18.0	308.0
18.5	308.0
19.0	313.0
19.5	324.0
20.0	325.0
20.5	352.0
21.0	374.0
21.5	406.0
22.0	433.0
22.5	459.0
23.5	517.0
24.5	569.0

Table A2 Reconstructed stagnation point thermocouple temperatures for the large probe

Time, s	Temperature, K (Uncoupled ablation)	Temperature, K (Coupled ablation)
18.0	311.4	306.0
18.6	315.5	309.8
18.8	316.4	311.3
19.2	317.8	314.7
19.5	318.9	317.8
19.7	319.8	320.3
20.0	321.8	325.1
20.4	327.4	334.0
21.5	363.9	382.4
22.5	421.8	451.8
23.5	480.7	521.7
24.5	528.2	578.6

B. Carbon Phenolic Material Properties

The carbon phenolic material properties and decomposition kinetic model are presented below.

Table A3 Virgin material thermal conductivity [29]

Temperature, K	Thermal conductivity, W/m/K
256	0.561
311	0.636
367	0.693
422	0.742
477	0.774
533	0.774
589	0.742
644	0.698
700	0.630
811	0.479

Table A4 Char material thermal conductivity [29]

Temperature, K	Thermal conductivity, W/m/K
278	0.810
556	0.872
811	0.935
1089	0.977
1366	1.128
1645	1.189
1782	1.314
1923	1.502
2200	2.065
2478	2.790
2617	3.002
2756	3.502
3030	4.880
3311	6.390
3555	7.380
3778	9.325

Table A5 Virgin and char material enthalpy [29]

Temperature, K	Virgin material, J/kg	Char material, J/kg
200	-466151	-83184
400	-240609	115635
600	53873	372279
800	389902	672546
1000	769145	1059913
1200	1191632	1418062
1400	1657362	1783797
1600	2166334	2227869
1800	2718551	2635562
2000	3314010	3037998
2200	3952713	3516826
2400	4634659	3908132
2600	5359848	4333604
2800	6128280	4758706
3000	6939956	5238940
3200	7794875	5689954
3400	8693037	6103055
3600	9634443	6535009
3800	10619091	7043045
4000	11646983	7558289

Table A6 Pyrolysis gas enthalpy [29]

Temperature, K	Enthalpy, J/kg
298	0.0
500	725718
700	1639273
1000	3596248
1500	6606912
2000	8696912
2500	11295220
3000	17082987
3500	31175677
4000	51560601
4500	73843273

The rate of decomposition of each constituent i of the carbon phenolic material (resin and fiber) was assumed to take the form [30]:

$$\frac{\partial \rho_i}{\partial t} = B_i \exp\left(-E_i/(RT)\right) \rho_{0,i} \left(\frac{\rho_i - \rho_{f,i}}{\rho_{0,i}}\right)^{\psi}$$

where the constants are provided in Table A7. The decomposition characteristics are implemented within the material response solver.

Table A7 Carbon phenolic material decomposition kinetic constants

Constituent i	B_i, s^{-1}	E_i/R, K	ψ	$\rho_{0,i}$, kg/m^3	$\rho_{f,i}$, kg/m^3	Reference
A (resin)	1.4×10^4	8560	3	324.36	0.0	[30]
B (resin)	4.48×10^9	20440	3	973.09	518.98	[30]
C (fiber)	0	0	0	1560.20	1560.20	[30]

In the above, the minimum reaction temperature for constituents A and B were assumed to be 555 K and 333 K, respectively. The emissivity and absorptivity of carbon phenolic were assumed to be 0.7 [5]. The heats of formation of the virgin plastic and char were assumed to be -372.0×10^3 J/kg and 0 J/kg, respectively [5].

Acknowledgments

This work was funded by the NASA Space Technology Mission Directorate Entry Systems Modeling (ESM) Project. The authors thank Christopher Johnston and Andrew Hinkle of the Aerothermodynamics Branch at NASA Langley Research Center for their assistance.

References

[1] Seiff, A., Kirk, D. B., Young, R. E., Blanchard, R. C., Findlay, J. T., Kelly, G., and Sommer, S., "Measurements of Thermal Structure and Thermal Contrasts in the Atmosphere of Venus and Related Dynamical Observations: Results from the Four Pioneer Venus Probes," *Journal of Geophysical Research: Space Physics*, Vol. 85, No. A13, 1980, pp. 7903–7933. https://doi.org/10.1029/JA085iA13p07903.

[2] Page, W. A., and Woodward, H. T., "Radiative and Convective Heating During Venus Entry," *AIAA Journal*, Vol. 10, No. 10, 1972, pp. 1379–1381. https://doi.org/10.2514/3.6632.

[3] Sutton, K., "Coupled Nongray Radiating Flow About Ablating Planetary Entry Bodies," *AIAA Journal*, Vol. 12, No. 8, 1974, pp. 1099–1105. https://doi.org/10.2514/3.49419.

[4] Moss, J., Zoby, E., and Sutton, K., "A Study of the Aerothermal Environment for the Pioneer Venus Multiprobe Mission," AIAA Paper 77-766, June 1977. https://doi.org/10.2514/6.1977-766.

[5] Wakefield, R. M., and Pitts, W. C., "Analysis of the Heat-shield Experiment on the Pioneer-Venus Entry Probes," AIAA Paper 80-1494, July 1980. https://doi.org/10.2514/6.1980-1494.

[6] Zoby, E. V., Moss, J. N., and Sutton, K., "Approximate Convective-Heating Equations for Hypersonic Flows," *Journal of Spacecraft and Rockets*, Vol. 18, No. 1, 1981, pp. 64–70. https://doi.org/10.2514/3.57788.

[7] Falanga, R., and Olstad, W., "An Approximate Inviscid Radiating Flow-field analysis for Sphere-cone Venusian Entry Vehicles," AIAA Paper 74-758, July 1974. https://doi.org/10.2514/6.1974-758.

[8] Ahn, H.-K., Park, C., and Sawada, K., "Response of Heatshield Material at Stagnation Point of Pioneer-Venus Probes," *Journal of Thermophysics and Heat Transfer*, Vol. 16, No. 3, 2002, pp. 432–439. https://doi.org/10.2514/2.6697.

[9] Park, C., and Ahn, H.-K., "Stagnation-point Heat Transfer Rates for Pioneer-Venus Probes," *Journal of Thermophysics and Heat Transfer*, Vol. 13, No. 1, 1999, pp. 33–41. https://doi.org/10.2514/2.6426.

[10] Takahashi, M., and Sawada, K., "Simulation of Entry Flight Flowfield Over Four Probe Vehicles in Pioneer-Venus Mission," AIAA Paper 2002-0909, January 2002. https://doi.org/10.2514/6.2002-909.

[11] Garvin, J. B., Getty, S. A., Arney, G. N., Johnson, N. M., Kohler, E., Schwer, K. O., Sekerak, M., Bartels, A., Saylor, R. S., Elliott, V. E., et al., "Revealing the Mysteries of Venus: The DAVINCI Mission," *The Planetary Science Journal*, Vol. 3, No. 5, 2022, p. 117. https://doi.org/10.3847/PSJ/ac63c2.

[12] Tauber, M. E., Palmer, G. E., and Prabhu, D. K., "Stagnation Point Radiative Heating Relations for Venus Entry," NASA ARC-E-DAA-TN2887, January 2012.

[13] Thompson, K. B., Hollis, B. R., Johnston, K. B., Christopher O, Lessard, V. R., and Mazaheri, A., "LAURA User's Manual: 5.6," NASA/TM-2020-2220566, February 2020.

[14] Yee, H. C., "On Symmetric and Upwind TVD Schemes," NASA TM-86842, September 1985.

[15] Cheatwood, F. M., and Thompson, R., "The Addition of Algebraic Turbulence Modeling to Program LAURA," NASA TM 107758, April 1993.

[16] Johnston, C. O., and Brandis, A. M., "Modeling of nonequilibrium CO Fourth-Positive and CN Violet emission in CO_2-N_2 gases," *Journal of Quantitative Spectroscopy and Radiative Transfer*, Vol. 149, No. 1, 2014, pp. 303–317. https://doi.org/10.1016/j.jqsrt.2014.08.025.

[17] Erb, A. J., West, T. K., and Johnston, C. O., "Investigation of Galileo Probe Entry Heating with Coupled Radiation and Ablation," *Journal of Spacecraft and Rockets*, Vol. 57, No. 4, 2020, pp. 692–706. https://doi.org/10.2514/1.A34751.

[18] Johnston, C. O., Gnoffo, P. A., and Mazaheri, A., "Influence of Coupled Radiation and Ablation on the Aerothermodynamic Environment of Planetary Entry Vehicles," VKI Lecture STO-AVT-218, 2013.

[19] Mazaheri, A., Johnston, C. O., and Sefidbakht, S., "Three-Dimensional Radiation Ray-Tracing for Shock-Layer Radiative Heating Simulations," *Journal of Spacecraft and Rockets*, Vol. 50, No. 3, 2013, pp. 485–493. https://doi.org/10.2514/1.A32448.

[20] Johnston, C., Brandis, A., and Sutton, K., "Shock Layer Radiation Modeling and Uncertainty for Mars Entry," AIAA Paper 2012-2866, June 2012. https://doi.org/10.2514/6.2012-2866.

[21] Amar, A. J., Blackwell, B., and Edwards, J., "Development and Verification of a One-Dimensional Ablation Code Including Pyrolysis Gas Flow," *Journal of Thermophysics and Heat Transfer*, Vol. 23, No. 1, 2009, pp. 59–71. https://doi.org/10.2514/1.36882.

[22] Johnston, C. O., "Study of Aerothermodynamic Modeling Issues Relevant to High-Speed Sample Return Vehicles," VKI Lecture STO-AVT-218, 2014.

[23] Park, C., Jaffe, R. L., and Partridge, H., "Chemical-Kinetic Parameters of Hyperbolic Earth Entry," *Journal of Thermophysics and Heat Transfer*, Vol. 15, No. 1, 2001, pp. 76–90. https://doi.org/10.2514/2.6582.

[24] McBride, B. J., Zehe, M. J., and Gordon, S., "NASA Glenn Coefficients for Calculating Thermodynamic Properties of Individual Species," NASA/TP—2002-211556, September 2002.

[25] Keenan, J., and Candler, G., "Simulation of Graphite Sublimation and Oxidation Under Re-entry Conditions," AIAA Paper 94-2083, June 1994. https://doi.org/10.2514/6.1994-2083.

[26] Driver, D., and MacLean, M., "Improved Predictions of PICA Recession in Arc Jet Shear Tests," AIAA Paper 2011-141, January 2011. https://doi.org/10.2514/6.2011-141.

[27] Peterson, D. L., and Nicolet, W. E., "Heat Shielding for Venus Entry Probes," *Journal of Spacecraft and Rockets*, Vol. 11, No. 6, 1974, pp. 382–387. https://doi.org/10.2514/3.62085.

[28] Brewer, R., "Selection of a Heat Protection System for Venusian Entry," AIAA Paper 75-731, May 1975. https://doi.org/10.2514/6.1975-731.

[29] Sutton, K., "An Experimental Study of a Carbon-phenolic Ablation Material," NASA TN D-5930, September 1970.

[30] Rindal, R. A., Clark, K. J., Moyer, C. N., and Flood, D. T., "Experimental and Theoretical Analysis of Ablative Material Response in a Liquid-Propellant Rocket Engine," NASA CR-72301, September 1967.

[31] West, T. K., and Brandis, A. M., "Stagnation-Point Aeroheating Correlations for Mars Entry," *Journal of Spacecraft and Rockets*, Vol. 57, No. 2, 2020, pp. 319–327. https://doi.org/10.2514/1.A34602.